

Numerical Study on Flow Characteristics of Airfoil With Bionic Micro-Grooves

Zhenren Wu (✉ zhengren_wu@163.com)

North China Electric Power University School of Energy Power and Mechanical Engineering, Baoding

Yufei Yang

North China Electric Power University - Baoding Campus

Mei Liu

Department of Economic Management, North China Electric Power University, Baoding

Kaishun Zhang

Department of Power Engineering, North China Electric Power University, Baoding

Original Article

Keywords: Bionic micro-groove, Large eddy simulation, Flow characteristics, Aerodynamic performance

Posted Date: October 12th, 2020

DOI: <https://doi.org/10.21203/rs.3.rs-88806/v1>

License: © ⓘ This work is licensed under a Creative Commons Attribution 4.0 International License.

[Read Full License](#)

Title page

Numerical study on flow characteristics of airfoil with bionic micro-grooves

Zheng-Ren Wu, born in 1973, is currently a supervisor of master students of North China Electric Power University, mainly engaged in fluid dynamics theory and application research, *China*.

Tel: +86-13930854056; E-mail: zhengren_wu@163.com

Yu-Fei Yang, born in 1996, is currently a master candidate at North China Electric Power University, *China*.

E-mail: yyu_fei@163.com

Mei Liu, born in 1977, is currently teaching at North China Electric Power University, *China*.

E-mail: liumei_w@163.com

Kai-Shun Zhang received his master degree from North China Electric Power University, *China*, in 2019

E-mail: kaishun_zhang@163.com

Corresponding author: Zheng-Ren Wu E-mail: zhengren_wu@163.com

Numerical study on flow characteristics of airfoil with bionic micro-grooves

Zheng-Ren Wu¹ • Yu-Fei Yang¹ • Mei Liu² • Kai-Shun Zhang¹

Abstract: For the purpose of exploring the influence of the location of the bionic micro grooves on the flow characteristics of the airfoil, three airfoil models with bionic grooves were established according to the different positions of the bionic grooves. Large eddy simulation is used to numerically simulate the flow of different airfoils. Compared with the smooth airfoil, the flow characteristics and aerodynamic performance parameters of the bionic micro-groove airfoil are analyzed at 6° angle of attack, 24 m/s and 30 m/s speed. The results show that the three types of bionic grooved airfoil suppress the thickness and flow length of the separation zone, making the reattachment position of the separation zone more forward than that of the smooth airfoil, thus having different degrees of separation of the airfoil surface boundary layer. Control effect. In addition, the existence of bionic micro-grooves reduces the vortex structure in the near-wall zone, reduces the center height of the separation zone, and reduces the normal velocity gradient, which weakens the energy dissipation in the flow. Airfoil-H1 airfoil has the best flow characteristics and aerodynamic performance at 24 m/s, the drag reduction rate is the largest, reaching 16.99%, and the lift-to-drag ratio increases by 16.34%. The Airfoil-H2 airfoil has the best effect at 30 m/s, the drag reduction rate is the largest, reaching 18.09%, and the lift-to-drag ratio increases by 18.86%. Airfoil-H3 airfoil has a lower effect, but the effect becomes more pronounced as the speed increases. As the mainstream speed increases from 24 m/s to 30 m/s, the optimal airfoil will gradually transition from Airfoil-H1 airfoil to Airfoil-H2 airfoil regardless of flow characteristics or aerodynamic performance parameters. It is found that there is the best matching value between the location of the bionic groove and the mainstream speed, so that the groove can play the best improvement effect.

✉ Zheng-Ren Wu
Zhengren_wu@163.com

¹ Department of Power Engineering, North China Electric Power University, Baoding, 071003, China

² Department of Economic Management, North China Electric Power University, Baoding, 071003, China

Keywords: Bionic micro-groove • Large eddy simulation • Flow characteristics • Aerodynamic performance

1 Introduction

Airfoil drag reduction technology has been widely used in fluid machinery, aerospace, etc. Researchers have adopted various methods to achieve a more ideal drag reduction effect. The methods of controlling drag mainly include active control and passive control. The passive control technology is a small investment and effective method [1]. The more common passive control methods include vortex generator [2], bionic leading edge [3], serrated trailing edge [4] and bionic micro groove [5]. Researchers have conducted a lot of research on passive control technology. Some scholars have studied the control of vortex generators on the separation of airfoil boundary layer through experiments. Research shows that the vortex generator has a better drag reduction effect on the boundary layer at a suitable installation angle and installation position, and will reduce the separation vorticity of the airfoil [6]. Jumahadi et al. [7] studied the airfoil surface hybrid vortex generator and found that the hybrid micro vortex generator increased the lift by 21.2%, increased the drag by 11.3%, and increased the lift-to-drag ratio by at least 8.6%. Tian et al. [8] used numerical methods to study the aerodynamic characteristics of the imitated owl wing airfoil, and the results showed that the lift coefficient and stall performance of the imitated owl wing airfoil were improved, and the efficiency of the bionic airfoil blade was increased by 12%. Zou et al. [9] studied the flow separation of the front and rear edge sinusoidal wave-shaped airfoil, and showed that the front and rear edge modification would increase the fluid disturbance and delay the fluid separation on the airfoil surface. Xu Chengyu et al. [10] simulated the aerodynamic performance of the airfoil with the leading edge of the owl. The aerodynamic performance of the airfoil was improved, and the lift coefficient increased by 19.8%. Yang et al.

[11][12] studied the serrated trailing edge bionic airfoil by LES and showed that the relative tooth height of the trailing edge has a greater impact on the aerodynamic characteristics of the airfoil. In addition, the serrated trailing edge delays the separation of the boundary layer, which speeds up the intermixing of fluids in the wake area and the energy transfer. Zhang [13] studied the aerodynamic performance of serrated trailing edge airfoil blades, and found that the trailing edge serrations caused the fluid to generate vortex pairs near the trailing edge and weakened the spanwise correlation of the vortex structure near the trailing edge.

These drag reduction methods are currently undergoing mechanism research and discussion, and the engineering realization of the bionic micro-groove drag reduction technology is easier than other technologies, so it is a method worth exploring and applicable to practical engineering. People have analyzed and discussed micro-groove drag reduction from different angles. For the geometry of micro-structures arranged downstream, Walsh [14] found through experiments that when the dimensionless height of the groove $h^+ \leq 25$, the dimensionless spacing $s^+ \leq 30$, the longitudinal groove can bring a certain drag reduction effect. For the design of the lateral groove size, there is no good conclusion. From the research of Sutardi [15], Amy [16], Ching [17] and others, it is found that when $s^+ \leq 50$ and $h^+ \leq 30$, it has a good drag reduction effect. Song et al. [18] found through numerical simulation that the V-shaped ridge structure on the airfoil surface can significantly reduce the turbulence intensity and turbulent kinetic energy in the airfoil boundary layer, proving the drag reduction effect of the ridge structure. WU et al. [19] studied the influence of different groove structure sizes on NACA0012 airfoil turbulence resistance. Under the optimal structure, the drag reduction rate reached 9.65%, and found that there is an optimal value for the groove spacing. Shi [20] used the SST k-w turbulence model to numerically simulate the airfoil with grooved V-groove structure, and showed that the V-groove structure at the back of the suction surface has the greatest drag reduction effect, with a drag reduction rate of 16.2%. Aiming at the micro-groove drag reduction mechanism, Yuan [21] simulated a special airfoil for wind turbines with micro-grooves and found that the V-groove mainly achieved drag reduction effects by reducing the pressure difference resistance. Serson et al. [22] studied the method of wing span corrugation to improve the aerodynamic performance of the airfoil with the help of DNS method, and found that the corrugation would reduce the lift-drag ratio of the airfoil. Liu et al. [23] analyzed the

microstructure drag reduction mechanism from the perspective of entropy generation, and showed that the groove structure can reduce the entropy generation in the flow process. Domel et al. [24] arranged a new type of tooth structure on the suction side of the airfoil and found that the airfoil drag can be reduced, the lift increased, and the momentum loss in the boundary layer caused by wall friction can be supplemented. Zhang et al. [25] conducted a simulation study on the drag reduction effect of the micro-textured airfoil, determined its drag reduction effect, and proved the influence of the micro-texture layout on the airfoil surface that they summarized on the drag reduction effect. Harun et al. [26] conducted wind tunnel experiments on the oblique staggered groove structure on the airfoil surface and found that the convergent and divergent staggered groove structure will significantly change the turbulence characteristics and reduce the airfoil resistance. Chamorro et al. [27] studied the resistance changes of wind turbine airfoil blades partially covered with groove structure through wind tunnel tests. The study found that the groove can reduce the frictional resistance of the airfoil wall, and the reduction varies with the height and geometry of the groove, and the partial coverage of the airfoil blade surface with the groove is in some cases more effective than the complete coverage effective.

At present, the numerical simulation and experimental research of the bionic groove structure on the airfoil surface mainly focus on the amount of drag reduction, while the analysis of the drag reduction mechanism of the bionic groove structure on the airfoil surface is relatively small. This paper mainly studies the influence of the groove structure on the flow characteristics of the airfoil and its basic influence mechanism when the bionic micro grooves are arranged at different positions of the airfoil.

2 Numerical simulation method and model establishment

2.1 Governing equation

The Navier-Stokes equation is filtered in the Fourier space to obtain the LES governing equation used in the simulation. The filtered control equation is as follows:

$$\frac{\partial \bar{u}_i}{\partial x_i} = 0 \quad (1)$$

$$\frac{\partial}{\partial t} (\rho \bar{u}_i) + \frac{\partial}{\partial x_j} (\rho \bar{u}_i \bar{u}_j) = \frac{\partial}{\partial x_j} (\sigma_{ij}) - \frac{\partial \bar{p}}{\partial x_i} - \frac{\partial \tau_{ij}}{\partial x_j} \quad (2)$$

$$\sigma_{ij} = \left[\mu \left(\frac{\partial \bar{u}_i}{\partial x_j} + \frac{\partial \bar{u}_j}{\partial x_i} \right) \right] - \frac{2}{3} \mu \frac{\partial \bar{u}_l}{\partial x_l} \delta_{ij} \quad (3)$$

2.2 Geometric model and boundary conditions

The profile of the shark shield scale structure is adopted, and based on the analysis conclusions of Sutardi [15], Amy [16], Ching [17] and others on the dimension characteristics of the transverse groove, when the dimensionless height of the groove is $h^+ \leq 30$ And the dimensionless spacing $s^+ \leq 50$, the bionic groove structure can have a better drag reduction effect. Perform equal scaling on the shield scale contour curve.

Specify the dimensionless wall unit K:

$$K = \frac{v}{u_\tau} \quad (4)$$

$$u_\tau = \sqrt{\frac{\tau_w}{\rho}} \quad (5)$$

$$\tau_w = 0.0225 \rho U^2 \left(\frac{v}{U\delta}\right)^{0.25} \quad (6)$$

$$\delta = 0.37x \left(\frac{v}{Ux}\right)^{0.2} = 0.37x \text{Re}^{-0.2} \quad (7)$$

In the above formula, v is the fluid kinematic viscosity, m^2/s , u_τ is the airfoil wall shear velocity, m/s , τ_w is the airfoil wall shear stress, and ρ is the fluid density, kg/m^3 . According to dimensional analysis:

$$h^+ = \frac{h}{K} \quad (8)$$

$$s^+ = \frac{s}{K} \quad (9)$$

Select the bionic groove structure spacing $s=0.25$ mm, the groove height $h=0.11$ mm, and verify the bionic groove size. The results of calculating h^+ and s^+ for the two mainstream fluid velocities are shown in Table 1. From Table 1, it can be seen that the internal dimensionless parameters of the bionic groove structure meet the requirements at the two mainstream velocities.

Table 1 Dimensionless height and spacing of the grooves

Mainstream speed (m/s)	Re	h^+	s^+
24	1.6×10^5	8.9929	20.5161
30	2.0×10^5	10.9931	25.0793

This article is an airfoil with a bionic groove structure designed on the basis of NACA0012 airfoil, the airfoil chord length $C=100$ mm. Twenty bionic micro-grooves are arranged horizontally between the airfoil $0.35-0.40C$, $0.50-0.55C$, and $0.65-0.70C$ respectively, and they are

named Arifoil-H1 (abbreviated as H1) airfoil, Arifoil-H2 (abbreviated as H2) airfoil, Arifoil-H3 (abbreviated as H3) airfoil. The three-dimensional H2 airfoil geometry with bionic micro grooves is shown in Figure 1.

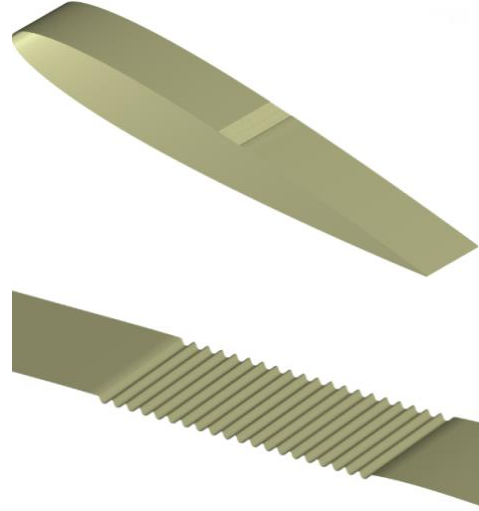


Figure 1 Schematic diagram of 3D bionic micro-grooved airfoil Arifoil-H2 model

The computational domain adopts a structured hexahedral grid. In order to ensure the quality of the grid near the airfoil, the computational domain adopts a C-type topology structure. The grid diagram is shown in Figure 2. And under the condition of $\text{Re}=1.6 \times 10^5$, the airfoil with bionic micro-groove structure arranged in $0.35C-0.40C$ was verified for grid independence. The three sets of meshes of this bionic micro-grooved airfoil are 1.255 million, 2.175 million and 3.45 million respectively. It can be seen from Table 2 that the difference in the time-average drag coefficient of the airfoil under the grid numbers of 1.255 million and 2.175 million is relatively large, while the relative change of the time-average drag coefficient of the airfoil under the grid numbers of 2.175 million and 3.45 million is very small. Considering the cost of numerical calculation while meshing quality, a bionic micro-grooved airfoil with 2.175 million meshes was selected for numerical simulation.

Table 2 Relation between mesh number and resistance coefficient

The grid number	C_d
1.255 million	0.02847253
2.175 million	0.02675768
3.45 million	0.02662551

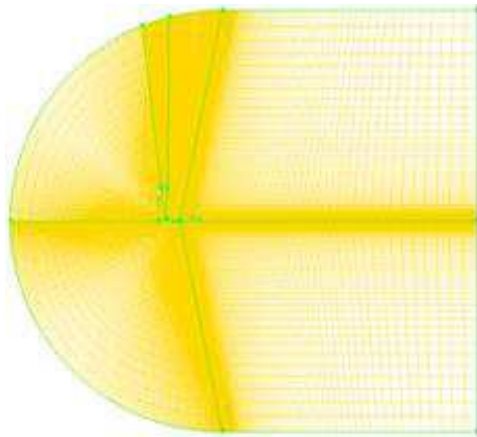


Figure 2 Bionic micro-grooved airfoil grid

The simulation adopts velocity-pressure coupling based on SIMPLEC algorithm, and the spatial discretization adopts the finite center difference format. First, the airfoil model is solved with 300-step steady-state solution using SST k- ω turbulence model; after the flow field reaches fully developed turbulence, the large eddy simulation (LES) method is used to perform 2000-step unsteady calculation of the flow field. The working fluid in the calculation domain is air, the air density is $\rho=1.225\text{kg/m}^3$, and the kinematic viscosity $\nu =1.5\times 10^{-5}\text{m}^2/\text{s}$. The airfoil headstream angle of attack is 6° , and the mainstream velocity $U=24\text{ m/s}$ and 30 m/s . The time step is $5\times 10^{-5}\text{ s}$, and the dimensionless wall height satisfies $y^+<1$.

2.2 Mechanism of the Exoskeleton Arm

According to the experimental conditions in reference [28], at 5° Angle of attack and 25 m/s velocity, the large eddy simulation was carried out for A smooth airfoil with chord length $C=100\text{ mm}$. The time-averaged pressure coefficient of the smooth airfoil wall was compared with the experimental data, and the results were shown in Figure 3.

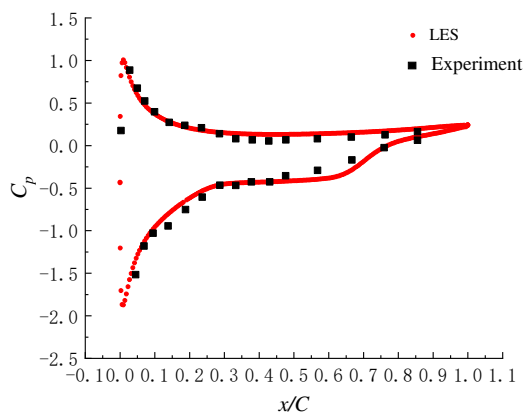
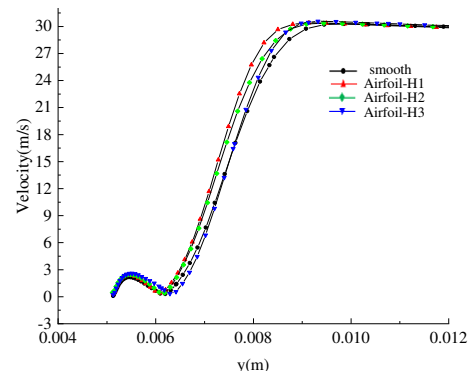


Figure 3 Comparison of time-averaged pressure coefficient of airfoil surface with experimental values

3 Results

3.1 Time-averaged velocity distribution of airfoil surface boundary layer

Figure 4 shows the time-averaged velocity distribution curve near the wall at different positions of the airfoil suction surface when $\alpha =6^\circ$, $U=24\text{ m/s}$, and 30 m/s . The speed change within the boundary at each position of the airfoil surface is basically the same at the two speeds. In Figure 4 (a) (c), that is, approximately in the middle of the separation zone, a more obvious boundary layer separation occurs and a recirculation zone is generated. Compared with the smooth airfoil, the speed of the recirculation zone is Figure 4 (b) (d) shows that at the position $x/C=0.675$, the reflux area of H1 and H2 airfoils has disappeared, and the fluid adheres to the airfoil surface again. The smooth airfoils and H3 airfoils are here. The boundary layer separation phenomenon still exists at the location. Moreover, the velocity near the wall of the three bionic grooved airfoils is significantly higher than that of the smooth airfoils. The difference is that when the speed increases from 24 m/s to 30 m/s , at the same chord length on each airfoil surface, the maximum time-average speed in the airfoil boundary layer changes from H1 airfoil to H2 airfoil. Moreover, when the H2 airfoil is at 30 m/s , the time-average speed is increased more significantly than when the H1 is at 24 m/s . As the speed increases, the H1 and H2 airfoils can still effectively shorten the range of the boundary layer separation section, and the effect of the H3 airfoil on improving the fluid flow characteristics is also obvious. At position $x/C =0.675$, H3 airfoil does not completely reattach the fluid to the airfoil surface like H1 and H2 airfoil, but it also reduces the thickness of the airfoil separation zone in the normal direction to a certain extent, so that the airfoil trailing edge flows. The situation is somewhat improved compared to the smooth airfoil.



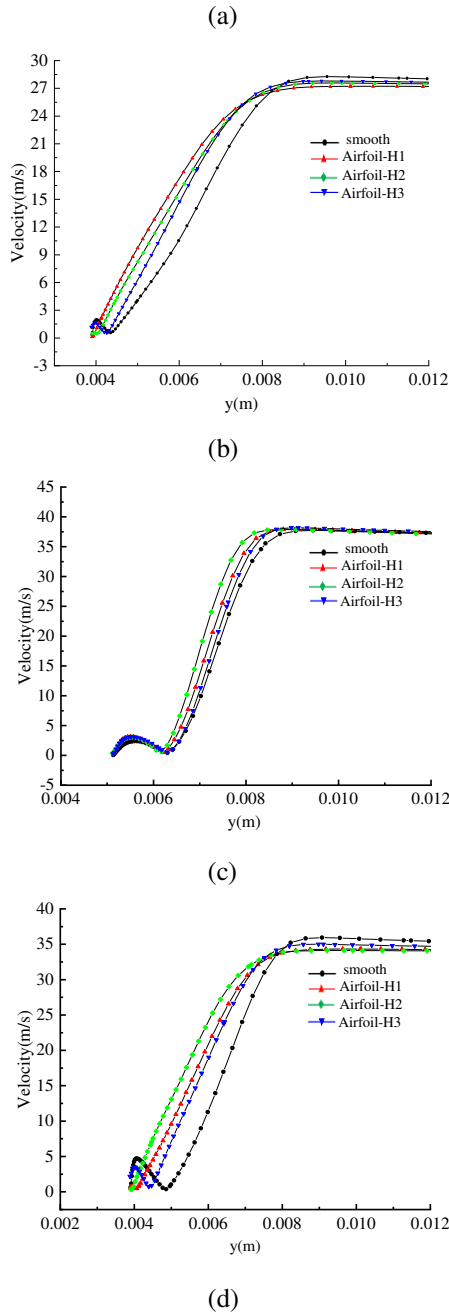


Figure 4 $u=24$ and 30 m/s, $\alpha=6^\circ$ Velocity distribution near the wall in the boundary layer at different positions of the airfoil:(a) $U=24$ m/s, $\alpha=6^\circ$ $x/C=0.525$;(b) $U=30$ m/s, $\alpha=6^\circ$ $x/C=0.525$;(c) $U=24$ m/s, $\alpha=6^\circ$ $x/C=0.675$;(d) $U=30$ m/s, $\alpha=6^\circ$ $x/C=0.675$

3.2 Time-averaged wall shear stress distribution of airfoil

The time-averaged wall shear stress distribution of a single bionic groove is shown in Figure 5. Figure 5(a) is a schematic diagram of the vortex structure in a single bionic groove. It can be seen from the figure that the vortex cannot fill the entire groove structure, and the vortex The contact area with the inner wall of the groove is limited

during rotation, so the shear stress of the inner wall of the groove structure is relatively smooth and the airfoil surface has a big change At two points A and B in the figure, the vortex structure is tangent to the groove wall, so the wall shear stress here is relatively large. Figure 5(b) shows the comparison between the time-averaged wall shear stress and the smooth airfoil in a single bionic groove. It can be seen from Figure 5(b) that the time-averaged wall shear stress of the groove structure is in the same section of the location area. The integral is its work value in the area, and its work is obviously smaller than that of a smooth airfoil, so the energy dissipation near the wall is correspondingly weakened.

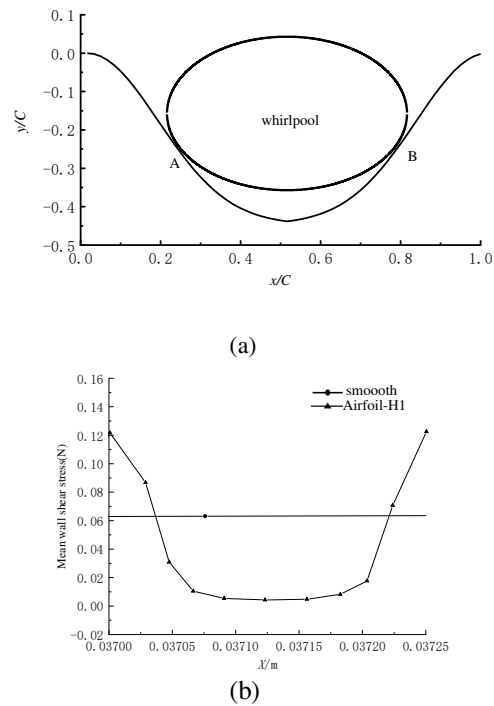


Figure 5 Schematic diagram of the vortex structure in a single bionic groove (L is the length of the groove) and the shear stress distribution on the wall in time

Table 3 shows the specific data of the average wall shear stress values of the three types of bionic airfoils H1, H2, and H3 and smooth airfoils at 24 m/s and 30 m/s. Figure 6 shows the comparison of the time-averaged wall shear stress values of the airfoil H1 and H2 with the smooth airfoil in the time-average velocity analysis results at 24 m/s and 30 m/s respectively. It can be seen from the figure that the time-averaged wall shear stress of the grooved structure section of the airfoil surface fluctuates regularly. The data in the table shows that under the same speed conditions, the mean value of the time-averaged wall

shearing is obviously smaller than the mean value of time-averaged wall shear stress of the smooth airfoil at the same position. This is because, compared to the stagnant velocity of the fluid on the smooth airfoil surface being reduced to zero, the fluid on the groove wall has a certain velocity at the groove port position, which reduces the normal velocity gradient in the near-wall area, thus the wall shear stress is reduced and the flow loss caused by

fluid viscosity is reduced.

At a speed of 30 m/s, the time-averaged wall shear stress of the H1 and H2 airfoil groove sections is slightly reduced compared with that at a speed of 24 m/s, but the change is not significant. In the surface groove section of the H3 airfoil, the average wall shear stress on the airfoil surface at 30 m/s is significantly larger than that at 24 m/s.

Table 3 Comparison of mean wall shear stress and smooth section in the bionic airfoil groove section

	Smooth-H1	Airfoil-H1	Smooth-H2	Airfoil-H2	Smooth-H3	Airfoil-H3
24 m/s	0.06384094	0.03516643	0.24912704	0.16201560	0.93062625	0.58229652
30 m/s	0.05747403	0.03487384	0.20853166	0.15628208	1.57385803	0.94850702

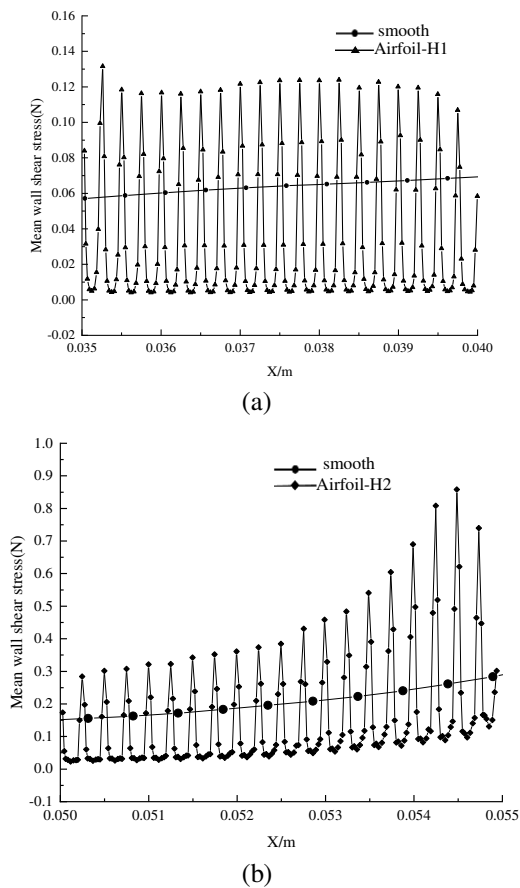
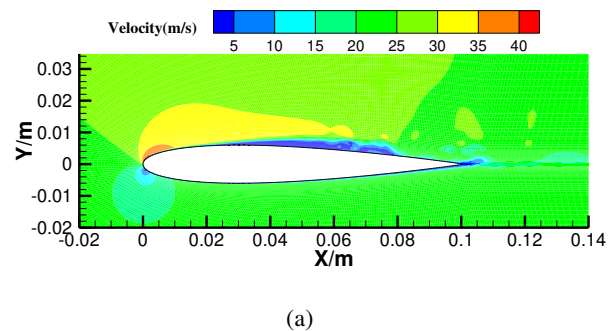


Figure 6 At different speeds, the time-averaged wall shear stress value of the bionic airfoil is compared with the smooth airfoil: (a) 24 m/s Airfoil-H1 airfoil; (b) 30 m/s Airfoil-H2 airfoil

3.3 Comparison of airfoil instantaneous velocity distribution

Figure 7 shows the instantaneous velocity cloud diagrams of the four airfoils at 6° angle of attack, 24 m/s and 30 m/s velocities. From Figure 7 (a), (c), (e), (g), it can be seen that the thickness and flow direction length of the separation zone on the upper surface of the smooth airfoil

are higher than the three bionic groove structures at an angle of attack of 6° and 24 m/s. The thickness and flow direction length of the H1 airfoil separation zone are the smallest. The reason for the backflow of the separation zone shows that at 24 m/s, the H1 airfoil has a better inhibitory effect on the thickness and flow length of the airfoil surface separation zone, and accelerates the early recovery of the separated fluid behind the airfoil suction surface. From Fig. 7 (b), (d), (f), (h), it can be seen that the thickness and flow direction length of the separation zone on the upper surface of the smooth airfoil are also the largest at a 6° angle of attack of 30 m/s. At this time, the thickness and flow direction length of the H2 airfoil separation zone are the smallest. It shows that at 30 m/s, the H2 airfoil has a better suppression effect on the thickness and flow direction length of the airfoil surface separation zone. H3 also has the same effect, but the suppression effect is weaker than the other two airfoils. The instantaneous velocity distribution and the range of the separation zone shown in each figure are confirmed by the conclusion obtained through the velocity distribution curve in Section 2.1.



(a)

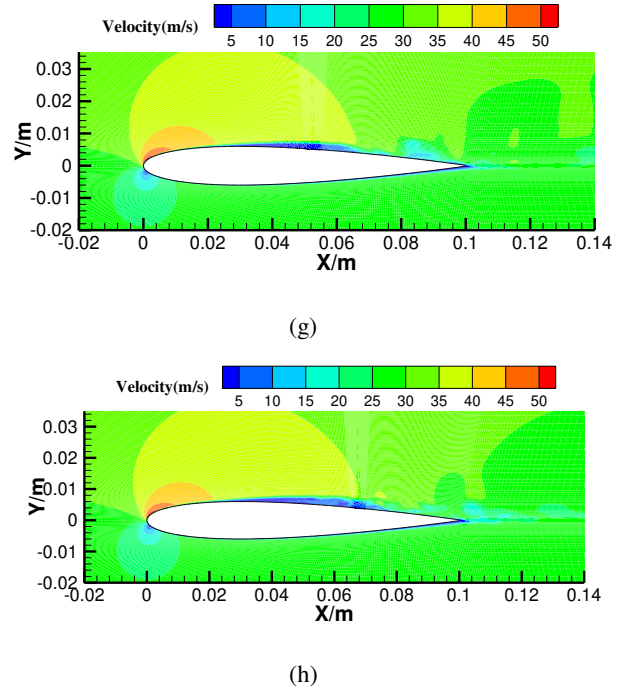
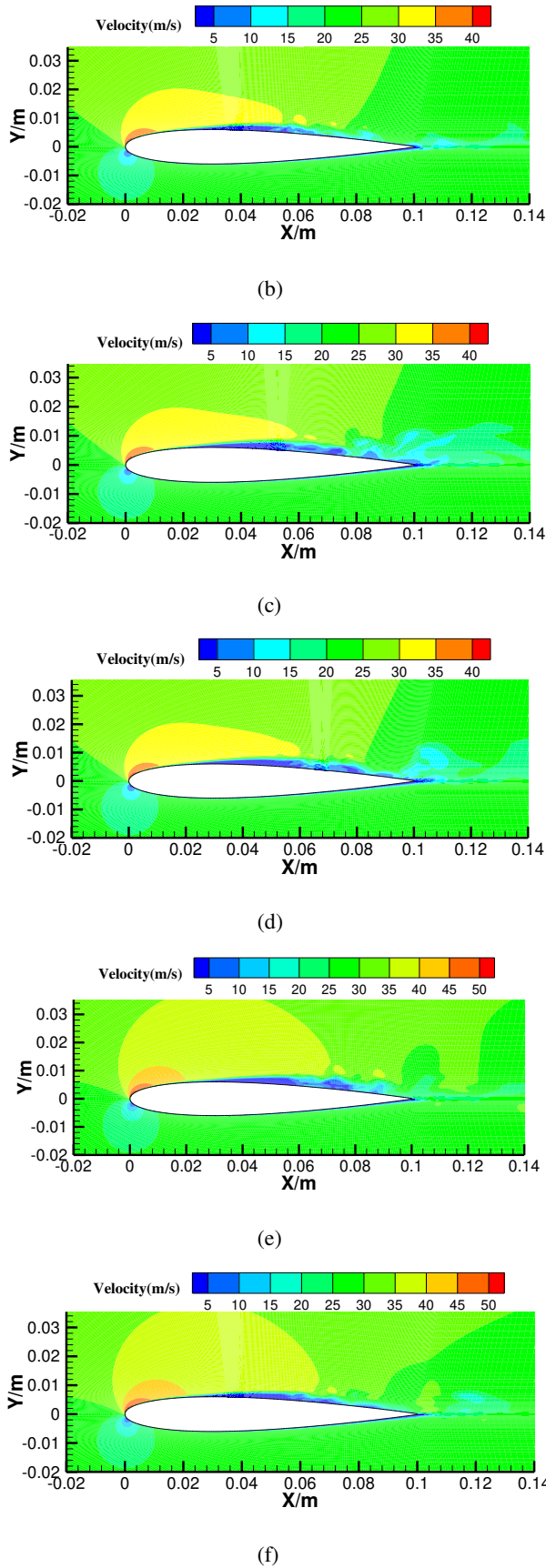


Figure 7 Instantaneous velocity cloud of airfoil: (a) $U=24$ m/s $\alpha=6^\circ$ smooth airfoil; (b) $U=30$ m/s $\alpha=6^\circ$ smooth airfoil; (c) $U=24$ m/s $\alpha=6^\circ$ Airfoil-H1 airfoil; (d) $U=30$ m/s $\alpha=6^\circ$ Airfoil-H1 airfoil; (e) $U=24$ m/s $\alpha=6^\circ$ Airfoil-H2 airfoil; (f) $U=30$ m/s $\alpha=6^\circ$ Airfoil-H2 airfoil; (g) $U=24$ m/s $\alpha=6^\circ$ Airfoil-H3 airfoil; (h) $U=30$ m/s $\alpha=6^\circ$ Airfoil-H3 airfoil

3.4 Time-averaged velocity distribution of airfoil surface boundary layer

According to the analysis of the previous sections, at 6° angle of attack, the airfoils with the best flow characteristics at 24 m/s and 30 m/s are H1 airfoils and H2 airfoils respectively. Therefore, at a speed of 24 m/s at an angle of attack of 6° , only the streamline diagram of the H1 airfoil and the smooth airfoil at the same position with a pulsating velocity cloud image is compared; at a speed of 30 m/s at a 6° angle of attack, only the H2 airfoil and the smooth airfoil streamline diagram with pulsating velocity cloud at the same position are compared, as shown in Figure 9.

In Figure 8 (a) and (c), there are obvious vortex structures at two positions on the smooth airfoil surface, while in Figure 8 (b) and (d), after the bionic groove structure is arranged at the same position, the two vortex structure disappeared obviously. And it can be seen from Fig. 8(a) and (b) that the height of the center of the airfoil boundary layer separation zone in the normal direction is significantly reduced. This shows that the existence of the bionic groove structure on the airfoil surface inhibits the generation and development of the wall vortex structure, significantly improves the fluid flow in

the near-wall region, and reduces the height of the main separation zone. The reduction in the height of the separation zone is beneficial to the fluid early reattachment on the airfoil surface.

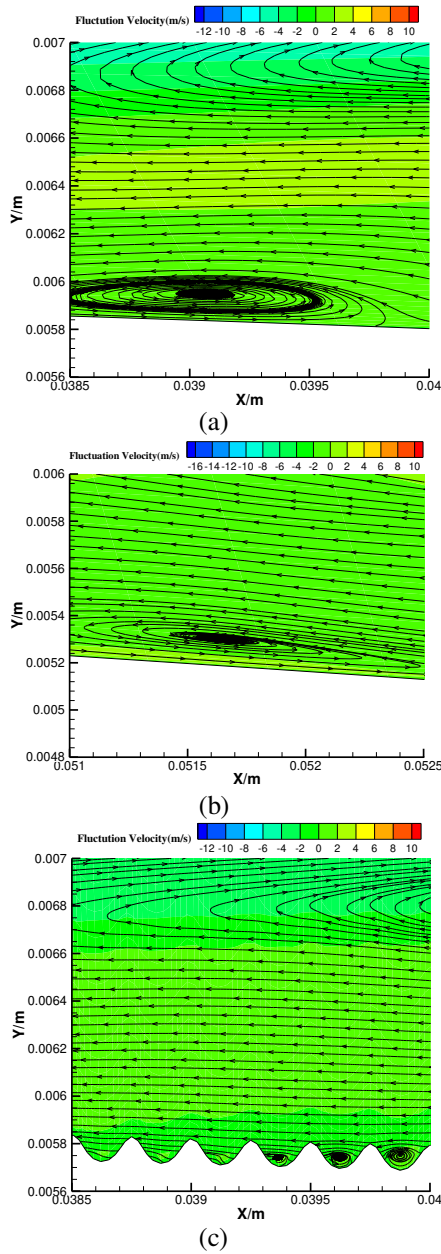


Figure 8 Comparison of streamline diagrams of different airfoils with pulsating velocity cloud diagrams at the same position: (a) $U=24$ m/s $\alpha=6^\circ$ smooth airfoil; (b) $U=30$ m/s $\alpha=6^\circ$ smooth airfoil; (c) $U=24$ m/s $\alpha=6^\circ$ Airfoil-H1 airfoil; (d) $U=30$ m/s $\alpha=6^\circ$ Airfoil-H2 airfoil

Figure 9 is the velocity vector diagram of the fluctuating velocity cloud diagram of the H3 airfoil groove at a speed of 6° angle of attack and 30 m/s. It can be seen from the figure that the fluid return zone has disappeared within a certain distance from the front end of the airfoil trailing edge, and the fluid flow direction has been consistent with the mainstream direction. And there is an obvious vortex structure in the groove. The fluid movement direction at the top of the vortex structure is consistent with the main flow direction. The vortex structure inside the groove continuously rotates, just like a "rolling bearing" transforms the sliding friction of the fluid near the wall into rolling friction. The analysis of section 2.2 reduces the wall shear stress and reduces the energy consumption caused by it.

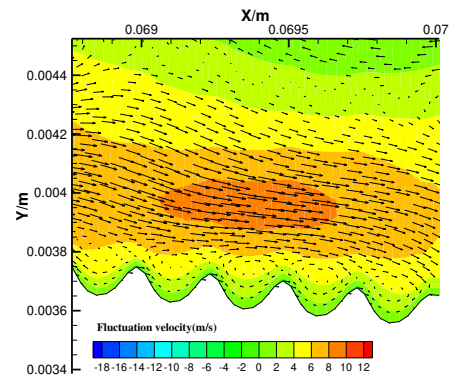


Figure 9 Airfoil-H3 airfoil groove part velocity vector diagram at 6° angle of attack and 30m/s speed

4 Analysis of aerodynamic performance of bionic airfoil

The bionic groove structure not only has a significant impact on the airfoil surface flow field, but also further changes the aerodynamics of the airfoil, and has a certain positive effect on it. Table 4 and Table 5 are the aerodynamic parameters of the airfoil at 6° angle of attack, 24 m/s and 30 m/s, respectively. It can be seen from Table 4 that the drag coefficients of the three bionic grooved structure airfoils at 24 m/s and 6° angle of attack are all reduced. Although the lift coefficient is slightly reduced, the lift-to-drag ratio is significantly increased. The H1 airfoil has the largest drag reduction rate, reaching 16.99%, and its comprehensive aerodynamic effect is the best among the three bionic grooved airfoils. Similarly, from Table 5, it can be seen that the drag coefficients of the three bionic grooved airfoils at 30 m/s and 6° angle of attack are also reduced, and the lift-to-drag ratio is also significantly increased, but at this time the H2 airfoil has the largest drag reduction rate, reaching 18.09%, and its comprehensive aerodynamic effect is the best among the three bionic grooved airfoils.

Table 4 Aerodynamic parameters of airfoil at 24 m/s and 6° Angle of attack

Model	Smooth	Airfoil-H1	Airfoil-H2	Airfoil-H3
Lift coefficient Cf	0.71666126	0.69205994	0.71199195	0.71124615
Drag coefficient Cd	0.03223572	0.02675768	0.02940479	0.02901203
Lift-to-drag ratio	22.232	25.864	24.213	24.516
Drag reduction rate	\	16.99%	8.78%	10.00%

Table 5 Aerodynamic parameters of airfoil at 30 m/s and 6° Angle of attack

Model	Smooth	Airfoil-H1	Airfoil-H2	Airfoil-H3
Lift coefficient Cf	0.71776140	0.70231026	0.69885661	0.71803846
Drag coefficient Cd	0.02916221	0.02560300	0.02388774	0.02657693
Lift-to-drag ratio	24.613	27.431	29.255871	27.017
Drag reduction rate	\	12.20%	18.09%	8.87%

In order to explore the influence of the speed change and the position of the bionic groove on the aerodynamic performance of the airfoil, numerical simulations were carried out on the H1 and H2 airfoil under the conditions

of 25.5 m/s, 27 m/s, and 28.5 m/s, and the aerodynamic performance was obtained. The parameter results are shown in Table 6. It can be seen from Table 6 that when the fluid velocity is 25.5 m/s, the comprehensive aerodynamic performance of the H1 airfoil is better than that of the H2 airfoil, and the lift-to-drag ratio is about 1.05% greater than that of the H2 airfoil. When the fluid velocity is 27 m/s, the lift-drag ratio of the H1 airfoil is only about 0.31% greater than that of the H2 airfoil. Compared with the case of 25.5 m/s, the gap between the two is further narrowed. When the fluid velocity is 28.5 m/s, the comprehensive aerodynamic performance of the H2 airfoil is better than that of the H1 airfoil. At this time, the lift-drag ratio of the H2 airfoil is about 1.74% greater than that of the H1 airfoil.

Combining Table 4 and Table 5, it can be inferred: when the speed is in the range of 24-27 m/s, the comprehensive aerodynamic performance of the H1 airfoil is better than that of the H2 airfoil; when the speed is in the range of 27-30 m/s (27 m/s is approximately the demarcation speed), the comprehensive aerodynamic performance of H2 airfoil is better than H1 airfoil. And when the speed increases from 24 m/s to 27 m/s, the comprehensive aerodynamic performance of the H1 airfoil gradually deteriorates, and the comprehensive aerodynamic performance of the H2 airfoil gradually improves. When the speed decreases from 30 m/s to 27 m/s, the comprehensive aerodynamic performance of the H2 airfoil gradually deteriorates compared to the H1 airfoil.

This shows that with the change of speed, the layout position of the bionic groove structure should also change, and there is an optimal matching value. At this time, the bionic groove structure airfoil can achieve the best comprehensive aerodynamic performance. The main trend is that as the mainstream speed increases, the bionic groove structure should gradually move backwards. The overall aerodynamic performance of the airfoil can be optimized when the incoming flow speed matches the location of the bionic groove.

Table 6 Aerodynamic parameters of Airfoil-H1 and Airfoil-H2 at 6° Angle of attack and other speeds.

	Model	Airfoil-H1	Airfoil-H2
25.5 m/s	Lift coefficient Cf	0.70256234	0.70135967
	Drag coefficient Cd	0.02660232	0.02683807
27 m/s	Lift-to-drag ratio	26.410	26.133
	Lift coefficient Cf	0.70199590	0.70663960
28.5 m/s	Drag coefficient Cd	0.02582147	0.02607130
	Lift-to-drag ratio	27.187	27.104
28.5 m/s	Lift coefficient Cf	0.69749537	0.70458745
	Drag coefficient Cd	0.02545105	0.02527155

Lift-to-drag ratio	27.405	27.881
--------------------	--------	--------

5 Conclusions

- (1) The three bionic grooved airfoils can effectively control the separation of the upper surface boundary layer of the airfoil, suppress the thickness and flow length of the separation zone, and make the airfoil boundary layer reattachment position more forward than the smooth airfoil. Airfoil-H1 works best when $U=24$ m/s, and Airfoil-H2 works best when $U=30$ m/s. Airfoil-H3 airfoil also has this effect, but compared with the first two airfoil, the effect is a little worse, and the effect is more obvious with the increase of speed.
- (2) Due to the existence of the bionic groove on the airfoil surface, the vortex structure in the near-wall zone is reduced, and the center height of the separation zone is reduced, and a small spanwise vortex structure is formed in the groove structure, which reduces the normal velocity gradient in the near-wall zone and reduces the wall surface. Shear stress weakens the energy dissipation in the flow process.
- (3) When the fluid velocity increases from 24 m/s to 30 m/s, it can be found that the airfoil with the best overall aerodynamic performance of the airfoil is similar to the change in flow characteristics and gradually transitions from Airfoil-H1 to Airfoil-H2. The overall trend is that the higher the mainstream speed, the more rearward the groove is arranged to improve the characteristics. It shows that the location of the bionic groove and the fluid velocity have an optimal matching value. Under different speed conditions, better results can be obtained by adopting the corresponding optimal layout position.

The research results of this paper have guiding significance for the optimization and layout design of the bionic micro grooves on the airfoil surface. But the disadvantage is that the data sample size is small, and the relationship between the mainstream velocity and the groove position cannot be accurately defined. Therefore, this is also the direction of improvement for our next research work.

7 Declaration

Acknowledgements

The authors sincerely thanks to Shuguang Li of North China Electric Power University for their critical discussion and reading during manuscript preparation.

Funding

This work was supported by the National Natural Science Foundation of Hebei Province, China (E2016502088) and The Fundamental Research Funds for the Central Universities, China (12QN39, 2015MS111).

Availability of data and materials

The datasets supporting the conclusions of this article are included within the article.

Authors' contributions

The author' contributions are as follows: ZW was in charge of the whole trial; YY wrote the manuscript; ML and KZ gave some advices on the manuscript. All authors read and approved the final manuscript.

Competing interests

The authors declare no competing financial interests.

References

- [1] S L Wang, Y H Deng, Z R Wu, et al. Advances in drag reduction of riblet surface. *China Sciencepaper*. 2016), 11(23), 2660-2666.
- [2] H Zhang, Z D Zhao, G X Zhou, et al. Experimental investigation of effect of vortex generator on aerodynamic performance of wind turbine airfoil. *Acta Energetica Solaris Sinica*, 2017, 38(04), 951-958.
- [3] Carlos A, Roberto M, Ragni D, et al. Boundary layer characterization and acoustic measurements of flow-aligned trailing edge serrations. *Experiments in Fluids*, 2016, 57(12):182-184.
- [4] F Avallone, D V W Van, D Ragni. Benefits of curved serrations on broadband trailing-edge noise reduction. *Journal of Sound and Vibration*, 2017, 400:167-177.
- [5] Z R Wu, X F He, R Rong, et al. Study on drag-reduction mechanism of riblet surface on airfoil blade of centrifugal fan. *Journal of System Simulation*, 2014, 26(6), 1355-1361.
- [6] X Q Du, Z Y Jiang, S X Tong, et al. Experimental study on control of separated flow over civil aircraft aft-body and drag reduction mechanism by using vortex generator. *Engineering Mechanics*. 2012, 29(8): 360-365.
- [7] M T Jumahadi, M R Saad, A C Idris, et al. The potential of hybrid micro-vortex generators to control flow separation of NACA 4415 airfoil in subsonic flow. *American Institute of Physics Conference Series*. 2018, doi: 10.1063/1.5022924.
- [8] W Tian, Z Yang, Q Zhang, et al. Bionic Design of Wind Turbine Blade Based on Long-Eared Owl's Airfoil. *Applied Bionics and Biomechanics*, 2017, 2017:1-10.
- [9] L Zou, Y F Lin. Numerical study of control mechanisms on flow past a modified airfoil. *Journal of Hydrodynamics*. 2012, 27(2), 117-123.
- [10] C Y Xu, Z H Qian, Q P Liu, et al. Aerodynamic performance of bionic coupled foils based on leading edge of long-eared owl wing. *Journal of Jilin University (Engineering and Technology Edition)*. 2010, 40(1),108-112.
- [11] J R Yang, A L Yang, E Y Chen, et al. Numerical research on aerodynamic characteristics and flow fields of airfoil with serrated trailing edge. *Journal of Aerospace Power*, 2017, 32(4), 900-908.

- [12] J R Yang, A L Yang, E Y Chen, et al. Research on the influence of airfoil performance with changing amplitude of Trailing Edge Serrations. *Energy Engineering*, 2016,(2),38-43.
- [13] X X Zhang, Numerical study on aerodynamics of the blades with serrated trailing-edge. University of Chinese Academy of Sciences. *Hefei: Institute of Engineering Thermophysics, Chinese Academy of Sciences*, 2013.
- [14] M Walsh. Turbulent boundary layer drag reduction using riblets. AIAA, Aerospace Sciences Meeting. *AIAA, Aerospace Sciences Meeting*, 1982, 769-787.
- [15] S Sutardi, W A Widodo. Analysis of Turbulence Characteristics in the Laminar Sub-Layer Region of a Perturbed Turbulent Boundary Layer. *Applied Mechanics and Materials*. 2016, 836: 115-120.
- [16] A W Lang, E M Jones, F Afroz. Separation control over a grooved surface inspired by dolphin skin. *Bioinspiration and Biomimetics*. 2017, 12(2), 026005.
- [17] Sutardi, C Y Ching. The response of a turbulent boundary layer to different shaped transverse grooves. *Experiments in Fluids*. 2003, 35(4), 325-337.
- [18] B W Song, Z Y Liu, H B Hu, et al. Numerical simulation study on drag reduction characteristics of airfoil surface ridge structure. *Chinese Journal of Computational Mechanics*, 2010, 27(5), 913-918.
- [19] Z R Wu, S G Li, M Liu, et al. Numerical research on the turbulent drag reduction mechanism of a transverse groove structure on an airfoil blade, *Engineering Applications of Computational Fluid Mechanics*, 2019, 13:1, 1024-1035.
- [20] Y L Shi. Study on drag reduction characteristics of surface structure of airfoil Special airfoil. Yangzhou: Yangzhou University, 2016.
- [21] Y P Yuan, H Yang, Y L Shi, et al. Study on drag reduction characteristics of airfoil for wind turbine with microgrooves on surface. *Journal of Engineering Thermophysics*, 2018, 39(06), 1258-1266
- [22] D Serson, J R Meneghini, S J Sherwin. Direct numerical simulations of the flow around wings with spanwise waviness at a very low Reynolds number. *Computers & Fluids*, 2017, 146,117-124.
- [23] M Liu, S G Li, Z R Wu, et al. Entropy generation analysis for grooved structure plate flow. *Elsevier Masson SAS*, 2019, 77,87-97.
- [24] A G Domel, G Domel, J C Weaver, et al. Shark skin-inspired designs that improve aerodynamic performance. *Journal of the Royal Society Interface*, 2018, 15(139), 20170828-1-20170828-9.
- [25] C Zhang, K S Bijay. Investigation on drag reduction performance of aero engine blade with micro-texture. *Aerospace Science & Technology*, 2018, 72, 380-396.
- [26] Z Harun, A Abbas, M Dhetaa, et al. Ordered roughness effects on NACA 0026 airfoil. *AEROTECH VI*. 2016.
- [27] P Chamorro, R Arndt, F Sotiropoulos. Drag reduction of large wind turbine blades through riblets: Evaluation of riblet geometry and application strategies. *Renewable Energy*, 2013, 50(3):1095-1105.
- [28] J L Qian, D F Wang. Experimental measurement and numerical simulation of aerodynamic characteristics of near-ground airfoils. *Chinese Journal of Hydrodynamics*, 2011, 26(2),150-156.

Biographical notes

Zheng-Ren Wu, born in 1973, is currently a supervisor of master students of North China Electric Power University, mainly engaged in fluid dynamics theory and application research, China.

Tel: +86-13930854056; E-mail: zhengren_wu@163.com

Yu-Fei Yang, born in 1996, is currently a master candidate at North China Electric Power University, China.

E-mail: yyu_fei@163.com

Mei Liu, born in 1977, is currently teaching at North China Electric Power University, China.

E-mail: liumei_w@163.com

Kai-Shun Zhang received a master's degree from North China Electric Power University, China, in 2019

E-mail: kaishun_zhang@163.com

Figures

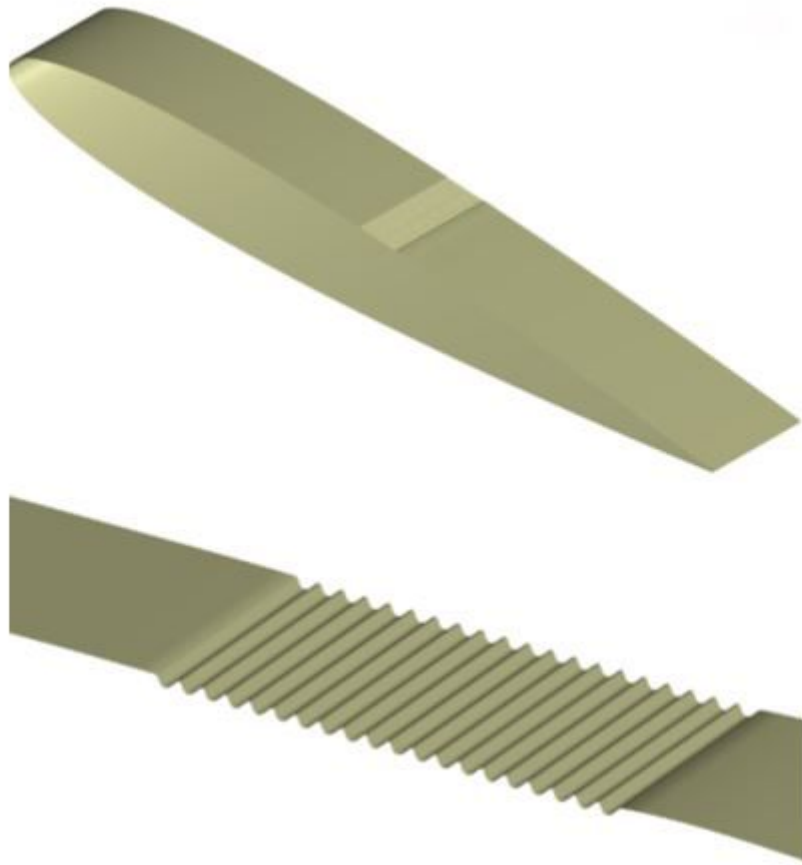


Figure 1

Schematic diagram of 3D bionic micro-grooved airfoil Arifoil-H2 model

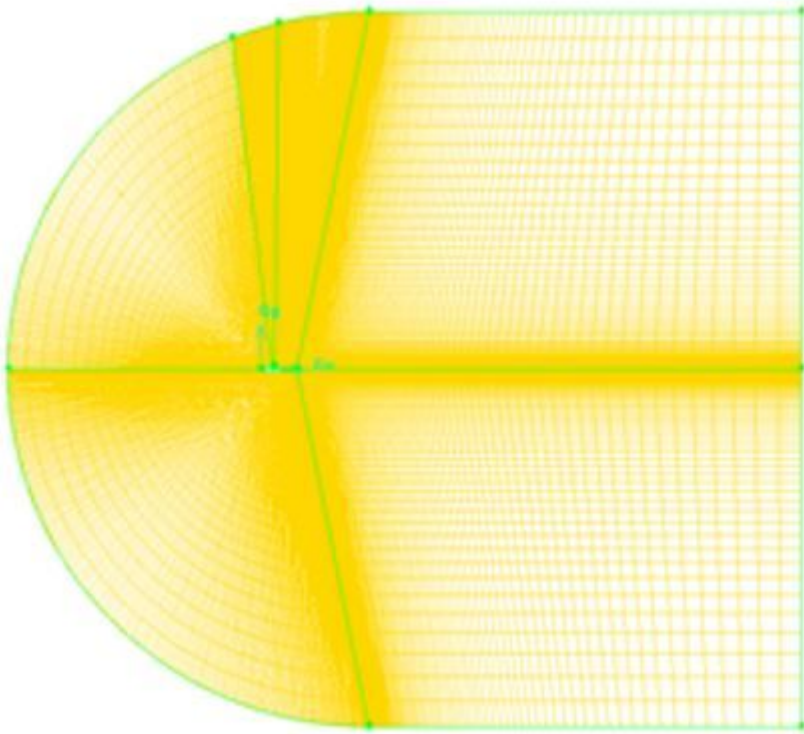


Figure 2

Bionic micro-grooved airfoil grid

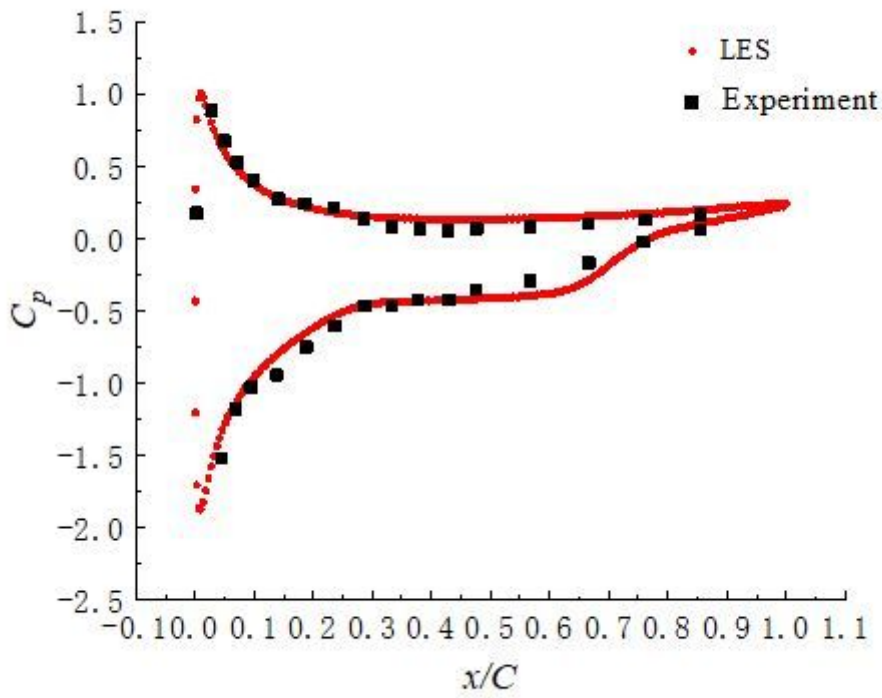
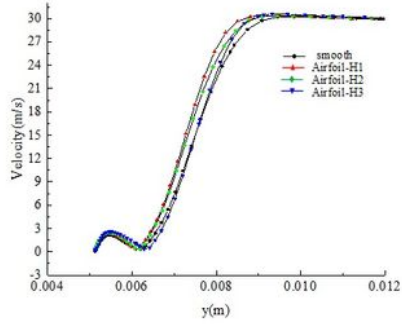
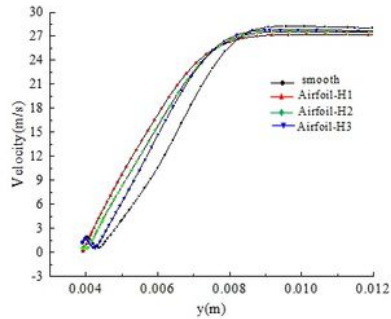


Figure 3

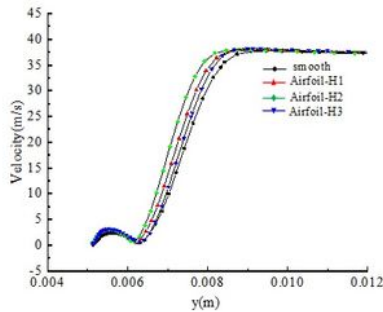
Comparison of time-averaged pressure coefficient of airfoil surface with experimental values



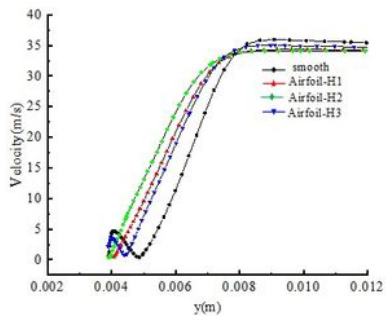
(a)



(b)



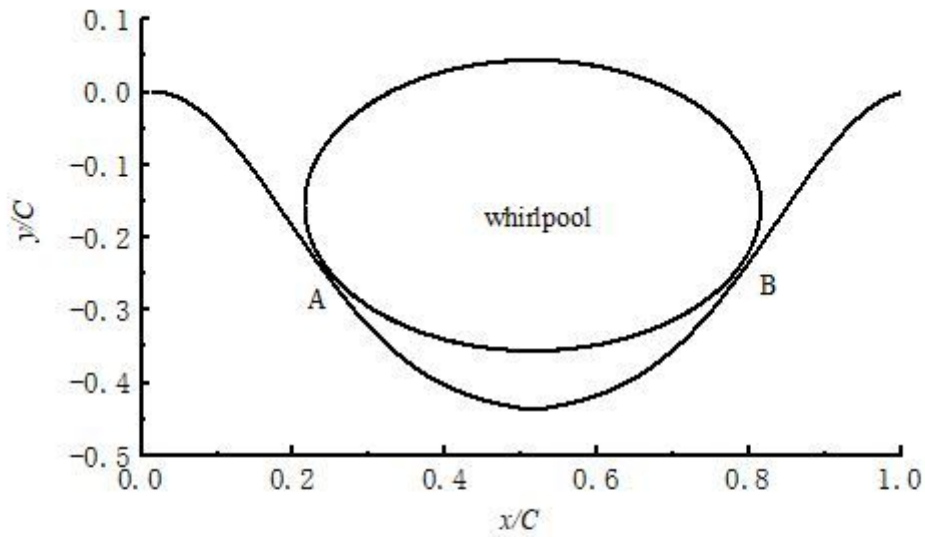
(c)



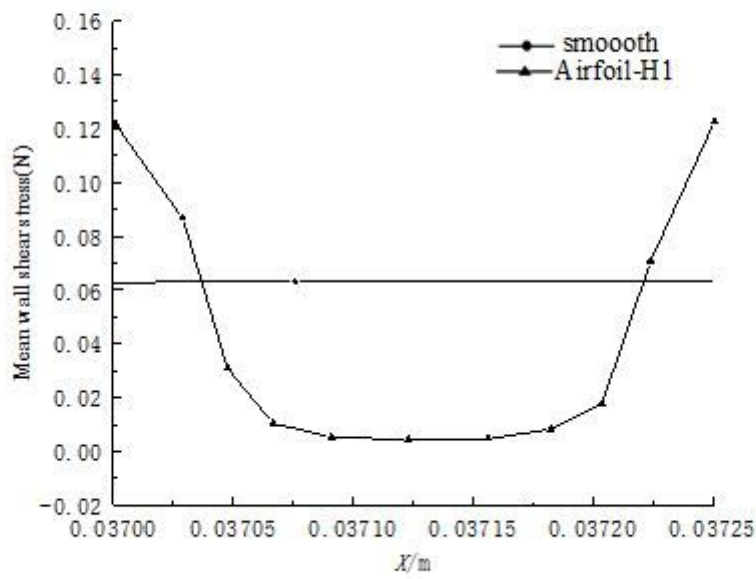
(d)

Figure 4

$u = 24$ and 30 m/s, $\alpha = 6^\circ$ Velocity distribution near the wall in the boundary layer at different positions of the airfoil: (a) $U = 24$ m/s, $\alpha = 6^\circ$ $x/C = 0.525$; (b) $U = 30$ m/s, $\alpha = 6^\circ$ $x/C = 0.525$; (c) $U = 24$ m/s, $\alpha = 6^\circ$ $x/C = 0.675$; (d) $U = 30$ m/s, $\alpha = 6^\circ$ $x/C = 0.675$



(a)



(b)

Figure 5

Schematic diagram of the vortex structure in a single bionic groove (L is the length of the groove) and the shear stress distribution on the wall in time

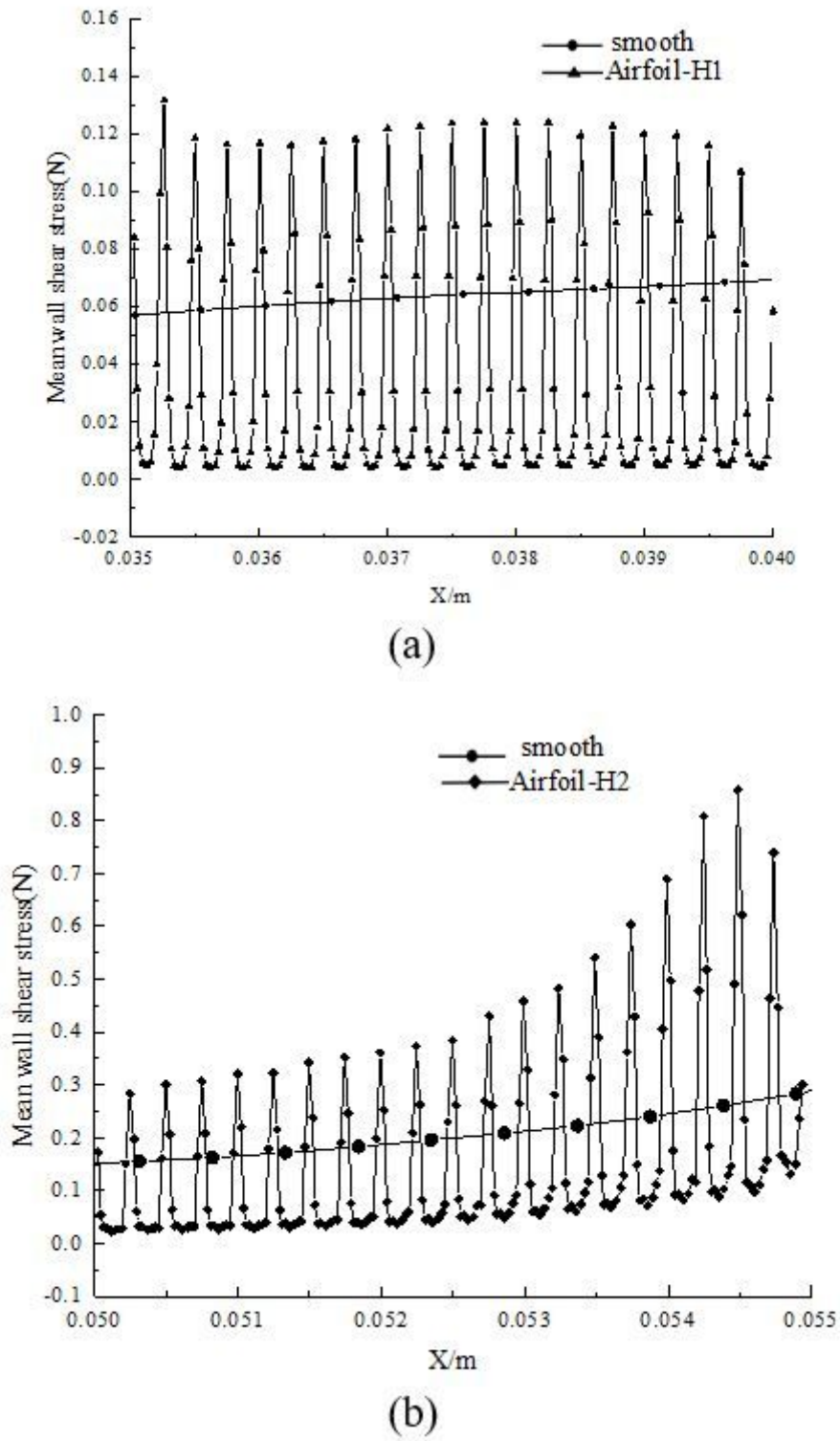


Figure 6

At different speeds, the time-averaged wall shear stress value of the bionic airfoil is compared with the smooth airfoil: (a) 24 m/s Airfoil-H1 airfoil; (b) 30 m/s Airfoil-H2 airfoil

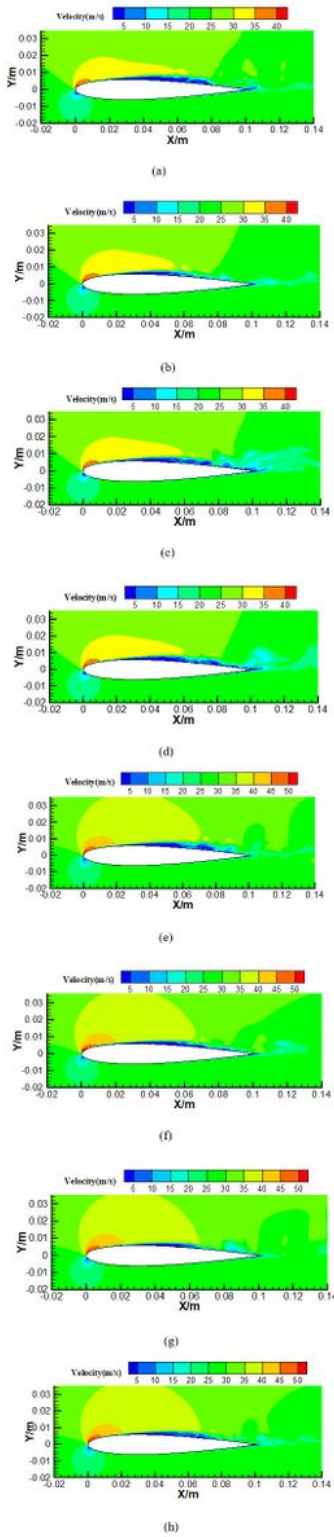
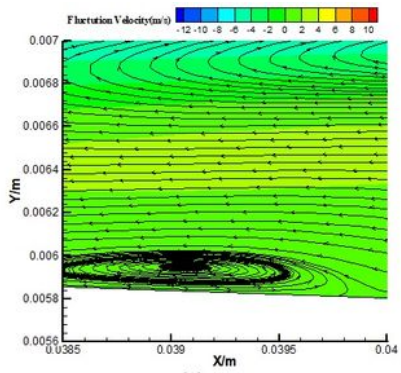
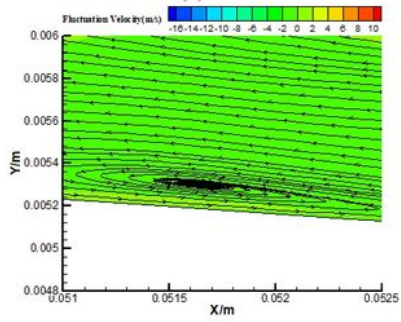


Figure 7

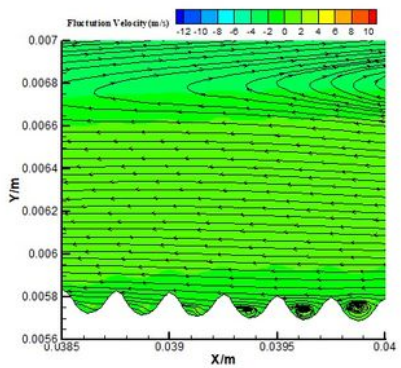
Instantaneous velocity cloud of airfoil: (a) $U=24$ m/s $\alpha=6^\circ$ smooth airfoil; (b) $U=30$ m/s $\alpha=6^\circ$ smooth airfoil; (c) $U=24$ m/s $\alpha=6^\circ$ Airfoil-H1 airfoil; (d) $U=30$ m/s $\alpha=6^\circ$ Airfoil-H1 airfoil; (e) $U=24$ m/s $\alpha=6^\circ$ Airfoil-H2 airfoil; (f) $U=30$ m/s $\alpha=6^\circ$ Airfoil-H2 airfoil; (g) $U=24$ m/s $\alpha=6^\circ$ Airfoil-H3 airfoil; (h) $U=30$ m/s $\alpha=6^\circ$ Airfoil-H3 airfoil



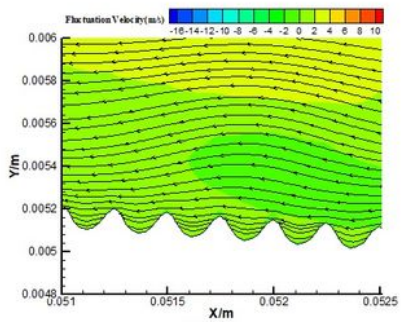
(a)



(b)



(c)



(d)

Figure 8

Comparison of streamline diagrams of different airfoils with pulsating velocity cloud diagrams at the same position: (a) $U=24$ m/s $\alpha=6^\circ$ smooth airfoil; (b) $U=30$ m/s $\alpha=6^\circ$ smooth airfoil; (c) $U=24$ m/s $\alpha=6^\circ$ Airfoil-H1 airfoil; (d) $U=30$ m/s $\alpha=6^\circ$ Airfoil-H2 airfoil

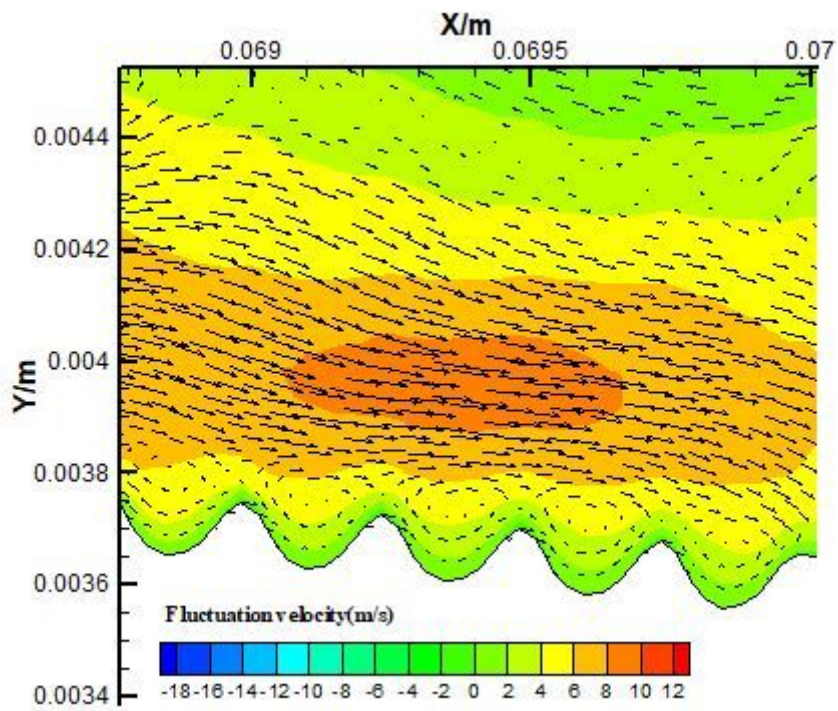


Figure 9

Airfoil-H3 airfoil groove part velocity vector diagram at 6° angle of attack and 30m/s speed